CRYSTAL GROWTH & DESIGN

pubs.acs.org/crystal

Article

Photoluminescent Nano-$CsPbBr_3$ Embedded in Cs_4PbBr_6 Crystals: Formation Mechanism and Properties

Weihao Sun, Yuan-Ting Hung, Wen-Tse Huang, Ru-Shi Liu,* and Wuzong Zhou*

Cite This: *Cryst. Growth Des.* 2024, 24, 545−553

Read Online

ACCESS | Metrics & More | Article Recommendations | Supporting Information

ABSTRACT: Luminescent crystalline cesium lead bromide has been synthesized by using an antisolvent method with the nominal ratio of Cs:Pb in the precursors varying in a wide range from 4.5:1 to 1:1. Although the powder X-ray diffraction patterns of all the specimens show Cs_4PbBr_6 as a pure phase or a main phase, high-resolution transmission electron microscopy images reveal a large amount of $CsPbBr_3$ nanocrystallites embedded in all the Cs_4PbBr_6 crystals. A formation mechanism of these perovskite nanocrystallites serving as actual active centers of photoluminescence is proposed. The most crucial step in the crystal growth is the deposition of a noncrystalline coating layer containing polymerized $PbBr_6^{4-}$ linked by Cs^+ with the Cs:Pb ratio of about 3:1, and therefore, the actual crystal growth sites are at the interface between the crystal and the coating layer, instead of the crystal/solution interface. The local lack of Cs during the formation of Cs_4PbBr_6 results in the formation of $CsPbBr_3$ nanocrystallites inside the parent crystals of Cs_4PbBr_6. The photoluminescence quantum yield and stability of the embedded $CsPbBr_3$ nanocrystallites are significantly improved in comparison with bare $CsPbBr_3$ crystals. Such simultaneous growth of parent crystals and the embedded nanocrystallites sheds light on further development of cesium lead halide-based photoluminescent materials.

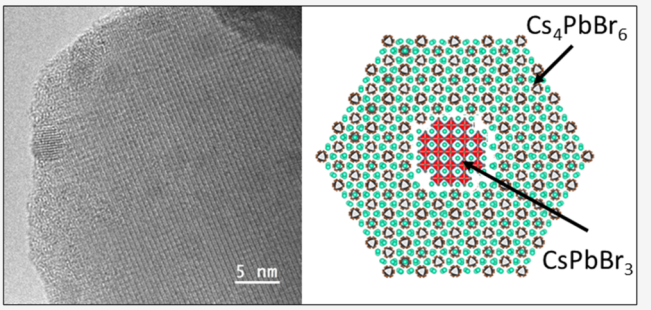

1. INTRODUCTION

In the past decade, cesium lead halide perovskite nanocrystallites ($CsPbX_3$, X = Cl, Br, and I) have drawn much attention from researchers because they are a promising candidate for next-generation light-emitting diode displays due to their high photoluminescence quantum yield (PLQY), narrow emission width, tunable emission wavelength, and facile synthesis protocol.[1−5] However, the vulnerability of $CsPbX_3$ to environmental elements such as moisture, heat, and UV light makes it harder to be commercialized.[6−8]

On the other hand, another ternary halide, Cs_4PbBr_6, has also been preliminarily suspected to have distinct green photoluminescence.[9] However, debates have existed for many years on the origin of its photoluminescence emission. Some people attributed this property to the intrinsic crystal structure of Cs_4PbBr_6,[10,11] while others argued that pure Cs_4PbBr_6 was nonluminescent.[12] Some people believed that there were luminescent $CsPbBr_3$ nanoparticles in the Cs_4PbBr_6 crystals. However, Seth and Samanta concluded that the photoluminescence of Cs_4PbBr_6 was due to some crystal defects rather than a secondary phase of $CsPbBr_3$ because the latter was not detected.[10] While many scientists insisted that the photoluminescence of the so-called Cs_4PbBr_6 was actually from coexisting $CsPbBr_3$ nanocrystallites, they were often not detectable by powder X-ray diffraction (XRD) or scanning electron microscopy (SEM).[13] In comparison with $CsPbBr_3$, Cs_4PbBr_6 exhibits higher chemical and thermal stabilities,[14,15] offering perfect protection to the photoluminescent nano-$CsPbBr_3$.

Without protection, the pure photoluminescent $CsPbBr_3$ quantum dots are thermally unstable and suffer decay in luminescence as time lengthens.[16,17] One way to overcome this shortcoming is to wrap these nanocrystallites using stable materials such as silica. Unfortunately, it was found that the $CsPbBr_3$@SiO_2 core−shell nanomaterials were poor emitters and degraded within minutes of exposure to ethanol, and further treatments were needed to improve their properties.[18] If the $CsPbBr_3$ nanocrystallites can be embedded in the Cs_4PbX_6 crystals to form a raisin bread-like structure via an one-step method, the stability and the luminescence property of $CsPbBr_3$ would be better maintained. In the development of these materials, direct observation of embedded $CsPbBr_3$ in Cs_4PbBr_6 crystals is crucial in understanding the luminescent nature of these materials.[19,20] The embedded nanocrystallites might not be detectable by powder XRD but could be detected by selected area electron diffraction (SAED) or high-resolution

Received: October 16, 2023
Revised: December 2, 2023
Accepted: December 4, 2023
Published: December 16, 2023

transmission electron microscopy (HRTEM) imaging, although these ternary halides are beam-sensitive. In our previous work, we demonstrated that it was possible to see the nanocrystallites of $CsPbX_3$ in Cs_4PbX_6 (X = Br or I) in HRTEM images directly.[21,22]

The previous research left a tricky problem, i.e., we did not know why the embedded $CsPbBr_3$ nanocrystallites formed during the growth of Cs_4PbBr_6 in an antisolvent precipitation method[23,24] and why their appearance was hardly affected by the precursor ratio of CsBr:$PbBr_2$. This lack of knowledge becomes a barrier in further investigation of cesium lead halide-based photoluminescent materials.

In the present work, we produced the Cs_4PbBr_6 rhombohedral microcrystals with embedded $CsPbBr_3$ nanoparticles with a large range of nominal ratios of CsBr:$PbBr_2$ in the synthesis solutions and other conditions being optimized. Their microstructures were characterized by using XRD, energy dispersive X-ray (EDX) spectroscopy, and HRTEM. A formation mechanism of the $CsPbBr_3$ nanocrystallites embedded in Cs_4PbBr_6 (designated as $CsPbBr_3$-in-Cs_4PbBr_6) crystals is proposed. The photoluminescence properties and stability of the produced materials were tested. With the passivation of Cs_4PbBr_6, the PLQY of the heterostructure material increases to 82% and has good resistance to high temperature and ultraviolet light.

2. EXPERIMENTAL SECTION

2.1. Materials. CsBr (Alfa Aesar, 99%), $PbBr_2$ (Alfa Aesar, 98%), 2-methylimidazole (MeIm, Aldrich, 99%), oleic acid (OA, Aldrich, 90%), oleylamine (OLA or OAm, Sigma-Aldrich), dimethylformamide (DMF, Acros Organics, 99+%), dimethyl sulfoxide (DMSO, Alfa Aesar, 99+%), toluene (Fluorochem, ≥ 99%), hexane (Fisher Scientific, laboratory reagent grade), isopropanol (Fisher Scientific, laboratory reagent grade), methanol (Fisher Scientific, ≥99.9%), acetone (Fisher Scientific, ≥99%), ethanol (VWR Chemicals), and deionized water (DI water) with a resistivity of 18.3 MΩ cm^{-1} were obtained. All chemicals were used as received without further purification.

2.2. Synthesis of Specimens. Cs_4PbBr_6 specimens were synthesized via an antisolvent precipitation method. The synthesis conditions including the concentrations of the solvent, ligands, *etc.* were varied, and optimized conditions were identified for achieving the most regular crystal morphology.

In a typical synthesis, a solvent combination of 10 mL of DMF and 10 mL of DMSO was preheated to 50 °C and kept stirring in an oil bath. 0.5 mmol (0.041 g) MeIm as well as 0.1 mL of OA and 0.5 mL of OLA were added into the solvent. 0.4 mmol (0.1468 g) $PbBr_2$ was added to the stirring solution, followed by addition of 1.6 mmol (0.3405 g) CsBr so as to keep the molar ratio of CsBr to $PbBr_2$ at 4:1. Different molar ratios (4.5:1, 3.5:1, 3:1, 2:1, and 1:1) of CsBr:$PbBr_2$ were applied based on the fixed molarity of $PbBr_2$ at 0.4 mmol. The solution was stirred for 1 h to guarantee total dissolution of the reactants.

When the stirring was accomplished, half of the solution was transferred into 10 mL of toluene under stirring. The mixture quickly turned into a white opaque suspension, which soon changed color to light green. After stirring for 5 min, the upper layer of the solution was removed, and another 10 mL of toluene was added into the precipitate-containing beaker. A second addition of toluene was not only for allowing further crystal growth but also for removing OA, OLA, and MeIm because the organic additives were also soluble in toluene. Then, the solid precipitate was isolated from toluene and put into an oven at 50 °C for drying. Finally, the dried sample was transferred to vials for further characterization. To test the effect from the polarity of the antisolvents, hexane, isopropanol, methanol, acetone, and ethanol were also used to replace toluene.

For synthesizing pure $CsPbBr_3$, 0.407 g of cesium carbonate (Cs_2CO_3) and 20 mL of 1-octadecene (ODE) were added to a 50 mL three-necked flask. In a vacuum system, the mixture was heated to 120 °C to remove water for 1 h. Then, under a nitrogen atmosphere, 1.25 mL of OA was injected into the solution, followed by further heating to 150 °C to allow the complete reaction between Cs_2CO_3 and OA. Before reacting with other reactants, the solution was heated to 120 °C until it became clear. To another 50 mL three-necked flask were added 20 mL of the ODE, 276 mg of lead bromide ($PbBr_2$), 2 mL of OA, and 2 mL of oleylamine (OAm). Under a vacuum condition, the mixture was heated to 120 °C to remove water for 30 min. Then, under a nitrogen atmosphere, the temperature was raised to 180 °C. After heating at this temperature for 10 min, 1.6 mL of Cs-oleate precursor was injected using a syringe. Waiting for 5 s after the injection, the three-necked flask was rapidly cooled in an ice−water bath to bring it to room temperature. Finally, the reacted specimen was centrifuged at 15 °C and 8000 rpm for 6 min. The precipitate was dispersed in either hexane or toluene for storage.

Characterization of specimens: Powder XRD was performed on a STOE diffractometer in Debye−Scherrer (capillary) mode at room temperature using Mo $K_{\alpha 1}$ (λ = 0.709 Å) radiation. The size of the capillary is 0.5 mm inner diameter. The diffracted X-rays were collected by using a scintillation position-sensitive linear detector. Samples were scanned in a range of 2θ from 5 to 30° for 2 h with a step size of 0.015°.

SEM images were recorded using a JEOL JSM-IT800 microscope operated from 5 to 15 kV. Samples were coated with a thin gold layer using a Quorum Technologies Q150RES sputter coater operated at 10 mA for 1 min to overcome the charging problem. EDX was performed on the same microscope at 15 kV. The samples for EDX were deposited on silica substrates instead of carbon tapes without gold coating to avoid signals from external carbon and gold.

TEM and HRTEM images were obtained using an FEI Titan Themis 200 S/TEM (in TEM mode) operated at 200 kV. Samples for TEM/HRTEM were dispersed in toluene and deposited onto TEM specimen grids coated with a holey carbon film before being put into the sample chamber. Short image acquisition time at 0.5 or 0.25 s was applied to avoid beam damage of the specimens.

The photoluminescence (PL), absorbance, excitation, and temperature-dependent PL spectra were all investigated using an FLS1000 photoluminescence spectrometer (Edinburgh). Internal quantum efficiency (IQE) data were obtained using an absolute PLQY spectrometer (Hamamatsu Photonics, C11347). The electroluminescence performance for the samples was acquired using a PMS-80 integrating sphere with an analyzer system (Everfine Photo-EINFO Co., Ltd.).

3. RESULTS AND DISCUSSION

The cesium lead bromide specimens with different nominal ratios of Cs:Pb = 4.5:1, 4:1, 3.5:1, 3:1, 2:1, and 1:1 were synthesized. During the synthetic process, CsBr and $PbBr_2$ were dissolved in the polar solvent to form a mother solution. A portion of the solution was then transferred into toluene, an antisolvent (organic solvents in which cesium lead bromides are insoluble, such as toluene, acetone, etc.). Due to the insolubility and ultimate supersaturation in the antisolvent, crystallization of Cs_4PbBr_6 or $CsPbBr_3$ would occur via the corresponding reactions of $4Cs^+ + Pb^{2+} + 6Br^- \rightarrow Cs_4PbBr_6$ and $Cs^+ + Pb^{2+} + 3Br^- \rightarrow CsPbBr_3$. From these reactions, a high ratio of CsBr to $PbBr_2$ would favor the formation of Cs_4PbBr_6, while a low ratio might result in the production of $CsPbBr_3$. Furthermore, producing a mixed phase of Cs_4PbBr_6 and $CsPbBr_3$ could be expected when the nominal ratio of CsBr to $PbBr_2$ was between 4:1 and 1:1. In practice, however, all the produced samples with the nominal ratio of CsBr to $PbBr_2$ from 4.5:1 to 1:1 led to a major phase of Cs_4PbBr_6, white in color,[25] which has a hexagonal unit cell with the

https://doi.org/10.1021/acs.cgd.3c01226
Cryst. Growth Des. 2024, 24, 545−553

parameters a = 13.73 and c = 17.32 Å (ICSD Code: 1538416). As shown in the XRD patterns (Figure 1), the specimens with

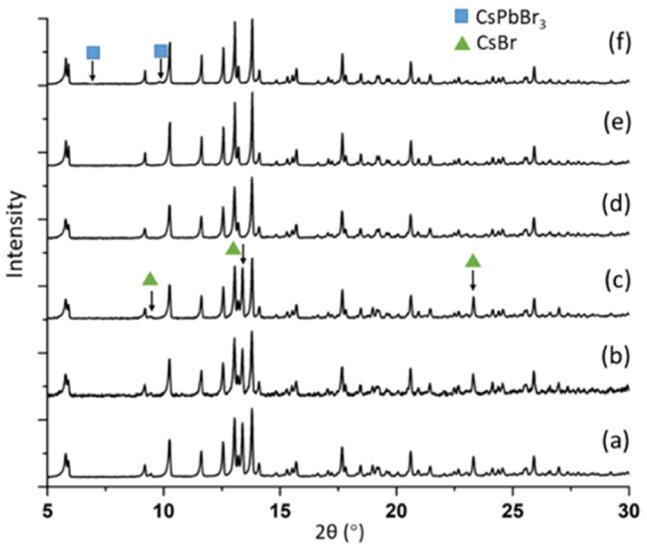

Figure 1. Powder XRD patterns (using Mo $K_{\alpha 1}$ radiation) of the produced cesium lead bromides with the nominal ratios of CsBr to $PbBr_2$ of (a) 4.5:1, (b) 4:1, (c) 3.5:1, (d) 3:1, (e) 2:1, and (f) 1:1. The green triangles in (c) indicate the diffraction peaks of CsBr. The blue squares in (f) indicate the peaks from cubic $CsPbBr_3$. All other peaks could be indexed to Cs_4PbBr_6.

the Cs:Pb nominal cation ratios of 4.5:1, 4:1, and 3.5:1 contain the major phase of Cs_4PbBr_6 with a minor phase of CsBr, which is cubic with the unit cell parameter a = 4.30 Å (ICSD Code: 236387). The actual composition of the major crystals had a ratio of Cs:Pb smaller than 4:1 as discussed below based on the EDX spectra. The reason for forming CsBr was simply because all Pb^{2+} cations were consumed during the formation of Cs_4PbBr_6 crystals and CsBr precipitated as a second solid phase.

The XRD patterns of the products corresponding to the Cs:Pb nominal ratios of 3:1 and 2:1 show a single phase of Cs_4PbBr_6. Only the sample with the Cs:Pb nominal ratio of 1:1 contains an extremely small proportion of cubic $CsPbBr_3$, which has a cubic perovskite structure with the unit cell parameter a = 5.87 Å (ICSD Code: 1533063) (Figure 1f). The $PbBr_2$ precipitate was never detected.

The structural models of Cs_4PbBr_6 and $CsPbBr_3$ are shown in Figure S1. Both structures can be regarded as constructions of $[PbBr_6]^{4-}$ octahedral clusters linked either by Cs^+ cations (in Cs_4PbBr_6) or by corner sharing (in $CsPbBr_3$). Other polymorphs of $CsPbBr_3$, i.e., the monoclinic and orthorhombic phases[26,27] were not observed in the present work when toluene was used as the antisolvent.

Pure Cs_4PbBr_6 is white and nonphotoluminescent under UV light and CsBr is also white, while pure cubic $CsPbBr_3$ is yellow and has green emission luminescence. The comparison of the colors and green-emitting properties under UV light of all of the samples can be a superficial way to distinguish the phases macroscopically. As shown in Figure 2, the white sample with the nominal ratio of Cs:Pb of 4.5:1 shows weak photoluminescence under UV light, indicating the existence of a small amount of $CsPbBr_3$. As the cation ratio decreases from 4.5:1 to 1:1, the color of the samples gradually changes from white to yellow, implying an increase of the $CsPbBr_3$ phase. The corresponding photoluminescence property was also enhanced with the decrease of the Cs:Pb ratio, although $CsPbBr_3$ was not detected from most samples by XRD.

The particle morphologies of all the samples were examined using SEM. The particles in 4.5:1 and 4:1 samples are small, a few hundred nanometers in diameter, and have irregular shapes (Figure S2a,b). The particle size in 3.5:1 and 3:1 samples

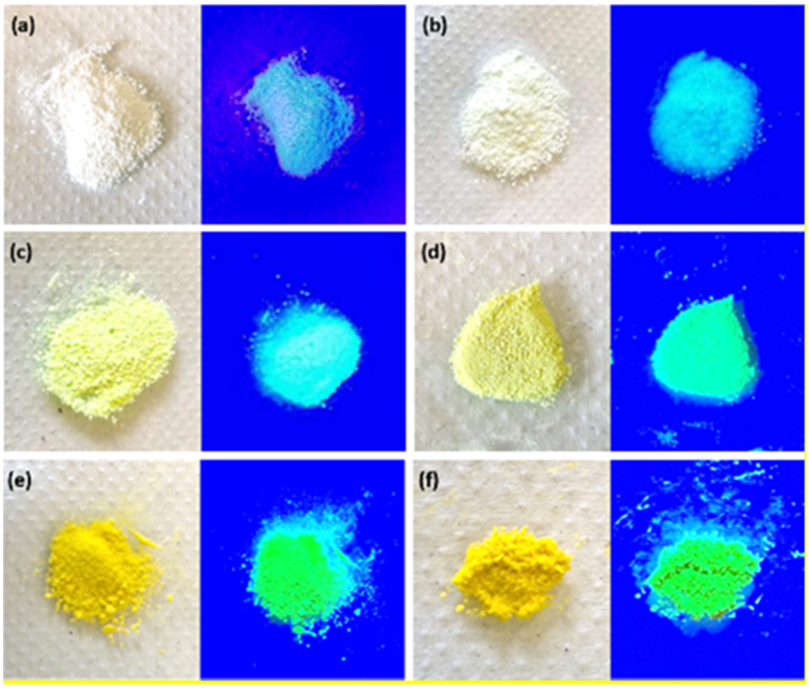

Figure 2. Photographs of the Cs_4PbBr_6 samples corresponding to the nominal ratios of CsBr to $PbBr_2$ at (a) 4.5:1, (b) 4:1, (c) 3.5:1, (d) 3:1, (e) 2:1, and (f) 1:1 under (left) visible light and (right) UV light (365 nm).

https://doi.org/10.1021/acs.cgd.3c01226
Cryst. Growth Des. 2024, 24, 545−553

increases to about 0.5 μm diameter, and some particles have a rhombohedral morphology (Figure S2c,d). A further decrease of the Cs:Pb ratios of 2:1 and 1:1 leads to a larger particle size of over 1 μm diameter and more regular rhombohedral morphology, which is the typical shape of Cs_4PbBr_6 crystals (Figure S2e,f). It is noted that the surface of these particles is quite clean without staining nanocrystallites.

TEM and HRTEM were applied to study the microstructures of the crystals. It was found that all of the crystals contain embedded nanoparticles. The sizes of these nanoparticles are similar in the different samples. We take the results from the 2:1 sample for discussion, in which most crystals show a rhombohedral morphology (Figure 3a). It can

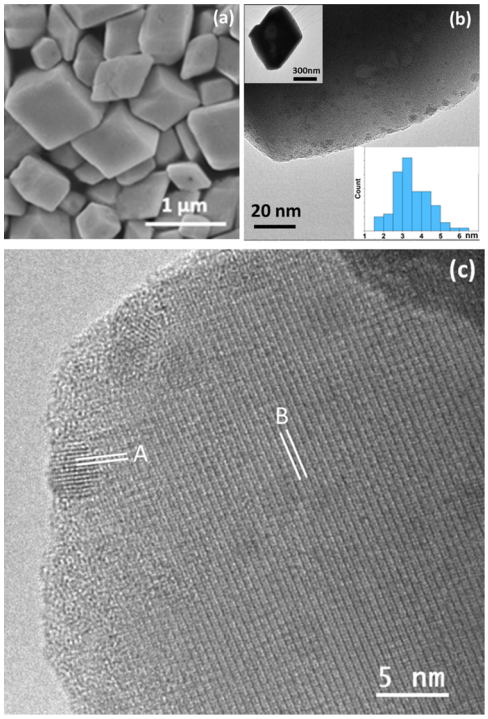

Figure 3. Microstructural analysis of the 2:1 sample. (a) SEM image of the Cs_4PbBr_6 particles. (b) Low-magnification TEM image of an edge of a particle. The top left inset is a TEM image of a whole rhombohedral particle. The bottom right inset shows the size distribution of the embedded $CsPbBr_3$ nanocrystallites, based on measurements of 200 dots. (c) HRTEM image showing (A) fringes with a d-spacing of 2.93 Å, which can be indexed to the (200) planes of $CsPbBr_3$, and (B) fringes with a d-spacing of 5.33 Å, which can be indexed to the $(\bar{1}103)$ planes of the Cs_4PbBr_6 host crystal.

be seen from TEM images that the crystals contain many embedded nanoparticles, as shown in Figure 3b. The image contrast agrees with the microstructures of the $CsPbBr_3$ nanoparticles in Cs_4PbBr_6. In other words, the darker contrast of the nanoparticles is due to a higher density of the heaviest atoms, Pb, generating a mass−thickness contrast in low-magnification TEM images. Majority of the nanoparticles have a diameter below 5 nm, and the average particle size calculated from 200 nanoparticles is about 3.5 nm diameter.

The crystals were very sensitive to the electron beam and decomposed in seconds under normal HRTEM conditions. However, if we prepared a dry sample and applied a very low dose of electron irradiation, it was still possible to obtain HRTEM intact structural images.[28] We have previously demonstrated successfully imaging of many beam-sensitive materials, including MOFs,[29] zeolites,[30] C_{60}/organic nanowires,[31] etc.

In the present work, some good HRTEM images were also recorded, which confirmed that the host crystals are Cs_4PbBr_6 and the embedded nanoparticles are $CsPbBr_3$. In Figure 3c, the fringes (A) in the marked nanoparticle have a d-spacing of 2.93 Å, which can be indexed to the (200) planes of $CsPbBr_3$. The fringes (B), covering a large area with a d-spacing of 5.33 Å, can be indexed to the $(\bar{1}103)$ planes of the hexagonal unit cell of Cs_4PbBr_6. The interplanar angle between these planes of two crystalline phases is measured to be 104°.

More HRTEM images showing fringes of both $CsPbBr_3$ and Cs_4PbBr_6 are shown in Figure S3. In particular, in Figure S3a, the fringes of 3.94 Å in the bulk crystal can be indexed to the $(03\bar{3}0)$ planes of Cs_4PbBr_6 and the fringes in the white dashed circle have a d-spacing of 4.16 Å, which can be indexed to the (110) planes of cubic $CsPbBr_3$. The interplanar angle of these planes of two different crystals is 45°.

This special angle ignited our speculation on their relation to crystal orientations. In the previous work, we observed evidence of epitaxial relation between Cs_4PbBr_6 and embedded $CsPbBr_3$, where the $[0001]_h$ axis of the former was parallel to the $[111]_c$ axis of the latter, where "h" and "c" represent hexagonal Cs_4PbBr_6 and cubic $CsPbBr_3$, respectively. This model gave a mismatch of +4.7% between $d_{10\bar{1}0(h)}$ and $3d_{110(c)}$. The mismatch between $d_{0001(h)}$ and $5d_{111(c)}$ was −2.1%.[21] The interplane angle between $(10\bar{1}0)_h$ and $(110)_c$ was 0 or 60°. The observed crystal orientations in Figures 3c and S3a cannot be explained by using this model.

The most possible model can be built with $[0001]_h//[001]_c$ and $[01\bar{1}0]_h//[100]_c$ as shown in Figure 4. In this case, $d_{0001(h)}$

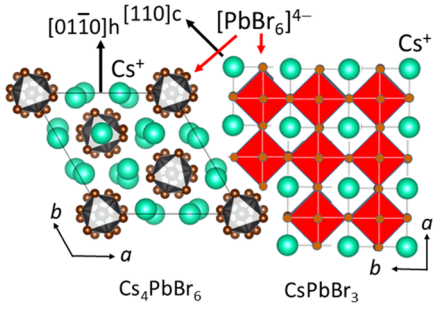

Figure 4. Schematic drawing of a proposed model to show the interface between Cs_4PbBr_6 and $CsPbBr_3$ when viewing down the [001] axes of both phases.

= 17.32 Å, $3d_{001(c)}$ = 17.61 Å, and the corresponding mismatch is +1.6%. Along the direction of $[01\bar{1}0]_h/[100]_c$, $d_{10\bar{1}0(h)}$ = 11.89 Å, $2d_{100(c)}$ = 11.74 Å, and the mismatching is −1.3%. This model has a smaller lattice tension at the interface of the two phases in comparison with the previously proposed model with $[0001]_h//[111]_c$.[21]

From this new model, the ideal interplane angle between the [110] zone axis of cubic $CsPbBr_3$ and the $[01\bar{1}0]$ axis of Cs_4PbBr_6 is 45°, which is the same as what we observed (Figure S3a). The observed interplane angle between the $[200]_c$ and $[\bar{1}103]_h$ zone axes is 104°, which is also close to the ideal interplane angle of 103° according to the model shown in Figure 4.

We have demonstrated how $CsPbBr_3$ nanocrystallites were embedded epitaxially within the Cs_4PbBr_6 host crystals in two

https://doi.org/10.1021/acs.cgd.3c01226
Cryst. Growth Des. 2024, 24, 545−553

manners, $[0001]_h//[111]_c$[21] and $[0001]_h//[001]_c$. The very good lattice matching enhances the stability of the cubic $CsPbBr_3$ and prevents its phase from decomposing or transforming to other nonluminescent polymorphs. However, this property does not help us to elucidate why the major phase in the products is always Cs_4PbBr_6 when the nominal ratio of Cs:Pb varies in a wide range from 4.5:1 to 1:1 and is why all the Cs_4PbBr_6 crystals contain $CsPbBr_3$ dots, forming the raisin bread-like structure (Figure S4). To reveal the formation mechanism of this structure, more detailed experimental data are required. The growth of Cs_4PbBr_6 rhombohedral crystals was very quick, making it difficult to obtain crystals chronologically and allocate the growth into different stages. Analysis is further performed on the mature crystals prepared under different conditions to infer what happens during the crystal growth.

Figure 5a shows a typical EDX spectrum of rhombohedral particles. The atomic ratio of Cs:Pb:Br is 3.1:1:6.7. The Cs:Pb

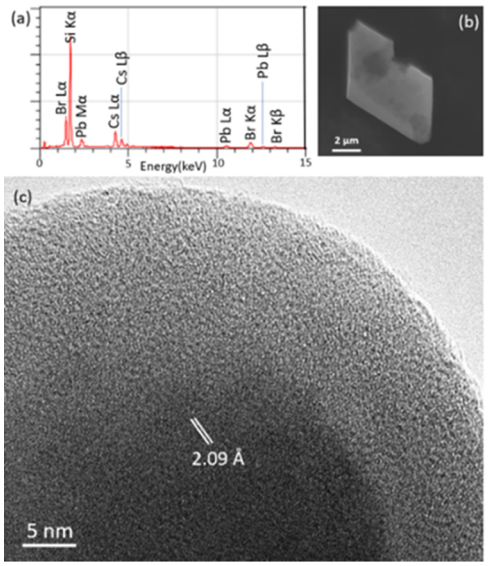

Figure 5. (a) EDX spectrum of a rhombohedral crystal, as shown in the SEM image (b). The Si peak was from the supporting substrate. (c) HRTEM image of a particle with interior crystalline fringes and a thick noncrystalline surface layer. The d-spacing of the fringes is marked.

ratios of all the rhombohedral crystals are between 3.1:1 and 3.9:1, with an average value of 3.5:1 from 20 particles. In comparison with the ideal formula of Cs_4PbBr_6 crystals, the Cs content is significantly lower and that of Br is higher. Figure 5c shows a crystal undergrowth with a thick disordered surface coating layer. The d-spacing measured from the crystal is 2.09 Å, which can be indexed to $(33\bar{6}4)$ of Cs_4PbBr_6. The image contrast of the coating layer is brighter than that of the crystal, implying that the coating layer has a lower density and/or contains lighter atoms. More importantly, the coating layer and the crystal do not have a clear boundary. Instead, there is a region at their interface that has a partially ordered structure. The crystallinity had a gradient change in this region. Such a disordered surface layer was detected in almost all particles, although their thickness was variable. The experimental observation implies that the coating layer and the crystal contain the same elements and even have similar compositions. The crystal growth sites are at the interface between the crystal and a disordered coating layer instead of the crystal/solution interface. Based on the properties discussed above, the disordered layers cannot be formed due to contamination of carbon under electron beam irradiation.

Based on the obtained experimental results, we are able to propose a formation mechanism of the $CsPbBr_3$-in-Cs_4PbBr_6 crystals (Figure 6), which allows us to explain the experimentally observed phenomena.

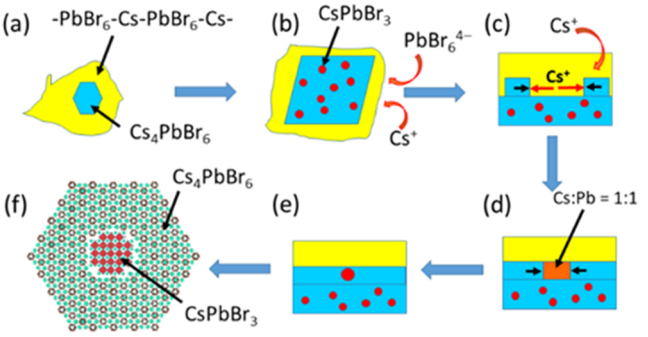

Figure 6. Schematic drawing of the proposed formation mechanism of $CsPbBr_3$-in-Cs_4PbBr_6 crystals. (a) Formation of the 3D polymerized bromide $-PbBr_6-Cs-PbBr_6-Cs-$ (yellow part) and nucleation of Cs_4PbBr_6 (blue part). (b) Deposition of a polymerized bromide coating on the crystal surface with an ideal ratio of Cs:Pb = 3:1. (c) Multiple crystal growth sites of Cs_4PbBr_6 at the interface between the crystal and the surface coating layer. (d) Extension of crystallization of Cs_4PbBr_6 on the crystal surface to leave an area with a ratio of Cs:Pb = 1:1 (brown part). (e) Formation of an embedded $CsPbBr_3$ nanoparticle (top red spot). (f) Epitaxial relation between the Cs_4PbBr_6 host crystal and an embedded $CsPbBr_3$ nanocrystallite.

When CsBr and $PbBr_2$ are dissolved in the DMF/DMSO solution of OA, OLA, and MeIm, both Cs^+ and Pb^{2+} cations bind with OA and OLA ligands (Figure S5) in this colorless transparent solution. The coupling effect of OA derives from the −COOH group, i.e., its dissociated −OH group, and the lone pair of electrons from ═O, while that of OLA derives from the lone pair of electrons in N. Additionally, the oxidation state of Pb^{2+} is higher than that of Cs^+, resulting in stronger confinement of Pb^{2+} by the bound ligands.

After the addition of toluene, the initial precipitated phase could be agglomerates of Cs^+ and Pb^{2+} cations with ligands, since both OA and OLA are polar molecules. The ligand molecules are soon replaced with Br^- anions. Although both CsBr and $PbBr_2$ are insoluble in toluene as a nonpolar solvent, these two solids did not precipitate first. The dominant phase in the precipitates is always Cs_4PbBr_6. It is proposed that Pb^{2+} cations form $PbBr_6^{4-}$ clusters, which are linked by Cs^+, forming polymerized bromide with a linkage of $-PbBr_6-Cs-PbBr_6-Cs-$. The linkage is not only one-dimensional (1D) but also can be two-dimensional (2D) and three-dimensional (3D) (Figure S6).

Nucleation of Cs_4PbBr_6 crystals then takes place in these agglomerates (Figure 6a), since the rearrangement of $PbBr_6^{4-}$ clusters and Cs^+ cations from the polymerized bromide to Cs_4PbBr_6 is relatively easy.

In the above-mentioned process, the antisolvent with a certain polarity plays an important role. A few common organic solvents were used as solvents or antisolvents in the present work, listed in the order of increase of their polarity indexes (in brackets): hexane (0.1), toluene (2.4), isopropanol (3.9),

https://doi.org/10.1021/acs.cgd.3c01226
Cryst. Growth Des. 2024, 24, 545−553

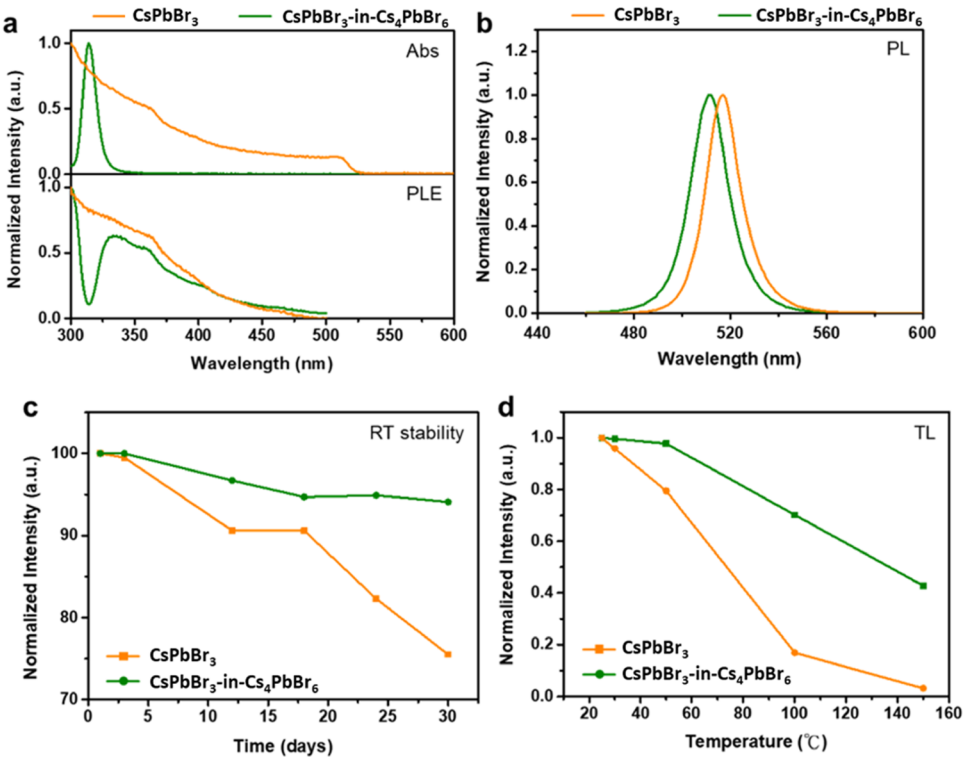

Figure 7. Optic properties of $CsPbBr_3$-in-Cs_4PbBr_6 and $CsPbBr_3$. (a) Normalized absorption and excitation spectra. (b) Normalized PL spectra. (c) PLQY test after storage under an ambident environment. (d) Temperature-dependent photoluminescence spectra measured from 25 to 150 °C.

methanol (5.1), acetone (5.1), ethanol (5.2), DMF (6.4), and DMSO (7.2).[32] CsBr and $PbBr_2$ are soluble in polar solvents (DMF, DMSO, etc.) but not soluble in nonpolar ones (hexane, toluene, isopropanol, acetone, etc.). It was expected that the solvents in the latter group could be used as antisolvents to achieve the precipitation of cesium lead halides from DMF/DMSO solutions. In practice, only toluene gave large regular rhombohedral Cs_4PbBr_6 crystals. Other solvents were used to replace toluene with the same amount, and the CsBr:$PbBr_2$ ratios were 2:1. Hexane, with a too big difference in the polarity index from that of DMF/DMSO, cannot mix with the DMF/DMSO solution, and therefore, no solid precipitates were produced. It seems to be essential to use an antisolvent with intermediate polarity in order to be compatible with the DMF/DMSO solution to induce the supersaturation and precipitation of halides. Using isopropanol, methanol, acetone, and ethanol, solid precipitates were observed. However, no products were monophasic rhombohedral Cs_4PbBr_6 crystals. Consequently, it was confirmed that toluene was the best antisolvent for producing Cs_4PbBr_6 crystals.

From the perspective of crystal growth, a fast growth rate or high supersaturation tends to create more nuclei and generate a smaller crystal size. In contrast, a slow growth rate or low supersaturation leads to fewer nuclei and larger crystal size. Furthermore, slow growth would form thermodynamically more stable regular polyhedra. The crystals we obtained show such a tendency indeed (Figure S2). On the other hand, even if the crystallization is very fast, the process via an intermediate disordered polymerized bromide phase is possible. A similar example is the growth of $CaCO_3$ crystals via amorphous calcium carbonate (ACC).[33] In addition, ionic polymers and oligomers have been identified to be prenucleation noncrystalline phases in many inorganic crystal growth processes.[34]

During the crystal growth of Cs_4PbBr_6, no matter whether the chemical spices approaching the crystals are Cs^+, Pb^{2+}, and Br^- free ions or cations with ligands or polymerized bromide, the crystal growth is not due to direct deposition of the ions into their crystallographic sites in Cs_4PbBr_6. Otherwise, some clean surfaces can be observed in the HRTEM images of Cs_4PbBr_6 crystals. In fact, the crystal surface is covered by a layer of disordered polymerized bromide (Figure 6b). If this soft bromide is based on $PbBr_6^{4-}$ octahedral clusters three-dimensionally linked by Cs^+, the ideal composition would approach $Cs_3PbBr_6^-$. The negatively charged coating layer would attract cations even with ligands and enhance the deposition of the disordered coating layer. The crystal composition detected by EDX has a Cs:Pb ratio higher than 3:1. This can be a result of some broken linkages of $Br_5Pb-Br-Cs$-Br-$PbBr_5$ into $Br_5Pb-Br-Cs$ and $Cs-Br-PbBr_5$ or due to the supplement of Cs^+ from the solution during the crystal growth.

With the microstructure described above, the crystallization sites would be multiple at the interface between the coating layer and the crystal surface (Figure 6c). The crystallization of Cs_4PbBr_6 needs a ratio of Cs:Pb = 4:1 and will generate many Cs vacancies in the surroundings. These vacancies would be filled by Cs^+ cations from the surrounding bromide and Cs^+ cations in the solution would migrate into the coating layer to supplement the Cs^+ concentration. When the crystallization extends two-dimensionally on a surface and the supplement of Cs^+ from the solution is not fast enough, some small areas with excess $PbBr_6^{4-}$ clusters would appear, finally forming spherical domains with a ratio of Cs:Pb of about 1:1, wrapped by the Cs_4PbBr_6 crystal (Figure 6d). These domains would then crystallize into $CsPbBr_3$ nanocrystallites (Figure 6e). Finally, a raisin bread-like structure forms with all the $CsPbBr_3$

https://doi.org/10.1021/acs.cgd.3c01226
Cryst. Growth Des. 2024, 24, 545−553

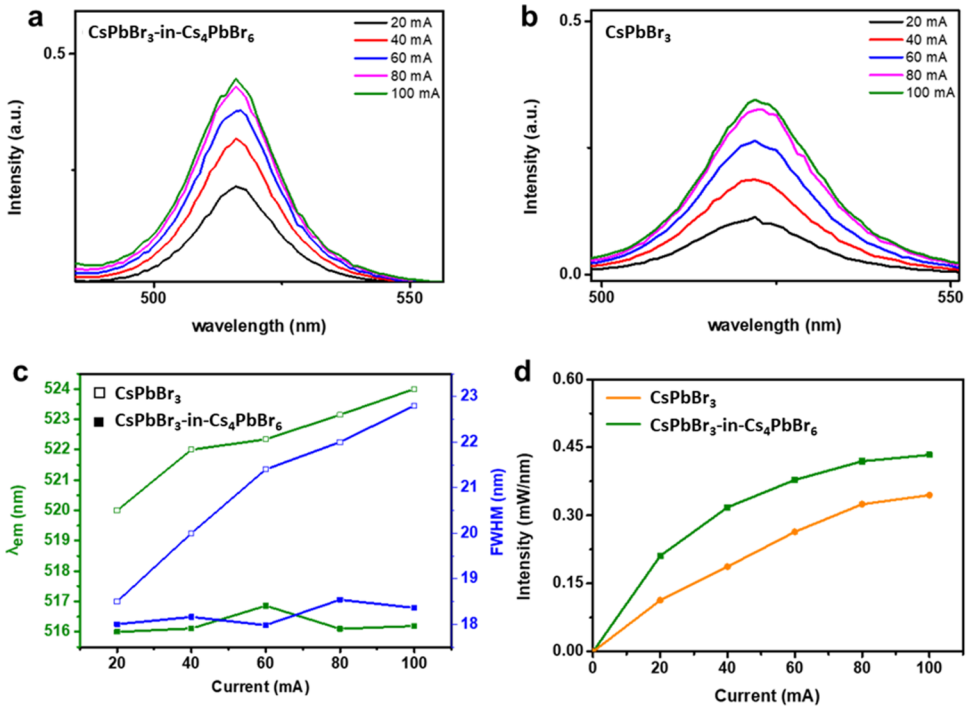

Figure 8. Luminous flux of (a) $CsPbBr_3$-in-Cs_4PbBr_6 and (b) $CsPbBr_3$ under different currents. (c) Emission wavelength (λ_{em}), full width at half maximum (FWHM), and (d) luminous flux of the two samples under different currents.

nanocrystallites inside the host crystals of Cs_4PbBr_6. In particular, when the two phases can self-adjust their orientations to achieve $[0001]_h//[100]_c$, the lattice tension at the interface of these two phases can be minimized and the stability of the $CsPbBr_3$ nanocrystallites would be improved (Figure 6f). Because of the continuous migration of Cs^+ from the solution to the particles, the final ratio of Cs:Pb is higher than 3:1, while with the existence of $CsPbBr_3$ nanocrystallites inside the particles, the overall ratio, Cs:Pb, of the particles, is smaller than 4:1.

To demonstrate the merits of $CsPbBr_3$-in-Cs_4PbBr_6 crystals, a pure cubic $CsPbBr_3$ specimen was synthesized as a reference. With a very low nominal ratio of Cs:Pb (~1:4), it is difficult to form 3D polymerized $PbBr_6^{4-}$ linked by Cs^+, leading to the formation of Cs_4PbBr_6. Its monophasic state and cubic structure were confirmed by XRD patterns as shown in Figure S7. To investigate the difference in optical properties of the $CsPbBr_3$-in-Cs_4PbBr_6 (nominal Cs:Pb = 2:1) and pure $CsPbBr_3$, the ultraviolet−visible (UV−vis) absorption spectra, photoluminescence excitation spectra (PLE), and PL spectra were recorded from these two samples. As shown in Figure 7a, the UV−vis absorption spectrum showed both $CsPbBr_3$' and $CsPbBr_3$-in-Cs_4PbBr_6's ability to absorb photons at different wavelengths. The PLE spectrum exhibited the material's capability to emit photons at different wavelengths when we monitored the emission at 520 nm for both samples. Both the PLE and UV−vis absorption spectra of $CsPbBr_3$ (orange) exhibited a consistent trend, which means that the energy in the wavelength range absorbed by $CsPbBr_3$ is released in the form of photons. In contrast, the PLE spectrum of $CsPbBr_3$-in-Cs_4PbBr_6 (green) exhibits a valley around 310−320 nm, while the absorption spectrum exhibited a sharp absorption peak attributed to the Pb^{2+} ion in isolated $[PbBr_6]^{4-}$ octahedra. The Pb^{2+} emission ($^1S_0 \rightarrow {}^3P_1$) can be observed under 10 K at 375 nm (strong excitation peak around 310 nm).[21,35] Moreover, the PLE spectrum trend of the $CsPbBr_3$-in-Cs_4PbBr_6 between 350 and 400 nm is similar to that of the $CsPbBr_3$, which suggests that the luminescence of $CsPbBr_3$-in-Cs_4PbBr_6 is derived from $CsPbBr_3$.

The PL spectrum of $CsPbBr_3$-in-Cs_4PbBr_6 exhibits a blue shift compared to that of pure $CsPbBr_3$. This phenomenon is probably due to the smaller size of the $CsPbBr_3$ nanoparticles inside the Cs_4PbBr_6 crystals than the particle size of pure $CsPbBr_3$ (Figure 7b).

Additionally, the PLQY values of the two samples were measured. The initial value of the PLQY for $CsPbBr_3$-in-Cs_4PbBr_6 was 82.7%, while that of the pure $CsPbBr_3$ sample was merely 66%. Moreover, the stability of these luminescent materials is also very important, allowing us to evaluate their subsequent applications. Both samples were stored under an ambient environment for one month. During this period, we measured the PLQY several times to monitor the change of the PLQY (Figure 7c). The $CsPbBr_3$-in-Cs_4PbBr_6 specimen showed better performance and higher stability than those of the pure $CsPbBr_3$ sample. This excellent property could be attributed to the passivation effect on the structure of $CsPbBr_3$ by the surrounding Cs_4PbBr_6 crystals. On the other hand, the perovskite $CsPbBr_3$ is vulnerable to the ambient environment. Without protection, the luminescent $CsPbBr_3$ crystals decompose gradually, losing their luminescence property.

The PL intensities of pure $CsPbBr_3$ and $CsPbBr_3$-in-Cs_4PbBr_6 with temperatures from 25 to 150 °C are shown in Figure S8. We can observe that the PL intensity decreases with the rise of the temperature for both samples. However, $CsPbBr_3$-in-Cs_4PbBr_6 can remain about 70% of its original PLQY under 100 °C, while pure $CsPbBr_3$ remains less than 20% PL intensity (Figure 7d).

To further investigate the application potential of these luminescent materials, $CsPbBr_3$-in-Cs_4PbBr_6 and $CsPbBr_3$ were deposited on a glass substrate to form films for testing

https://doi.org/10.1021/acs.cgd.3c01226
Cryst. Growth Des. 2024, 24, 545−553

the performance by blue LED backlighting. Figures 8a and 8b show the luminescence intensity of both samples under the variable current in the range from 20 to 100 mA. In any case, the luminescence intensity of $CsPbBr_3$ is always lower than that of $CsPbBr_3$-in-Cs_4PbBr_6. As shown in Figure 8d, when the current increases initially (0−40 mA), the luminescence intensity has an obvious increase as well. When the current further increases from 40 to 80 mA, the increasing trend of luminescence intensity gradually slows down. It seems to approach a constant value when the current is increased to 100 mA or above.

Additionally, we find that the emission position has a red shift and the FWHM broadens with increasing current for the pure $CsPbBr_3$ specimen, while for the $CsPbBr_3$-in-Cs_4PbBr_6 crystals, the emission position has almost no shift. This result shows that the $CsPbBr_3$-in-Cs_4PbBr_6 crystals have improved stability compared to $CsPbBr_3$ because the vulnerable perovskite $CsPbBr_3$ has been well-passivated by the surrounding Cs_4PbBr_6 crystal (Figure 8c).

4. CONCLUSIONS

In summary, Cs_4PbBr_6 crystals with embedded luminescent $CsPbBr_3$ nanocrystallites have been prepared with a large range of nominal ratios of the precursors, CsBr:$PbBr_2$, in a facile antisolvent method. The material has a high PLQY and better environmental stability than those of pure $CsPbBr_3$. Based on the microstructural analysis, a formation mechanism of this raisin bread-like structure is proposed. We believe that the crucial step in the construction of such a novel structure is the deposition of a polymerized bromide surface coating layer as an intermediate phase containing $PbBr_6^{4-}$ clusters linked by Cs^+ cations. The ideal Cs:Pb ratio of this three-dimensionally polymerized bromide is about 3:1. The crystal growth is, therefore, hardly affected by the nominal ratio of Cs:Pb. The present work sheds light on further control and development of cesium lead halide photoluminescent materials and fabrication of other raisin bread-like materials.

■ ASSOCIATED CONTENT

Supporting Information

The Supporting Information is available free of charge at https://pubs.acs.org/doi/10.1021/acs.cgd.3c01226.

Structural models of Cs_4PbBr_6 and $CsPbBr_3$, SEM images of the Cs_4PbBr_6 crystals, HRTEM images of Cs_4PbBr_6 crystals with embedded nano-$CsPbBr_3$, TEM images of Cs_4PbBr_6 crystals, binding of OA and OLA to Cs^+ and Pb^{2+} cations, polymerized $PbBr_6^{4-}$ linked by Cs^+, XRD pattern of the synthesized cubic $CsPbBr_3$, and temperature-dependent PL spectra of $CsPbBr_3$ and $CsPbBr_3$-in-Cs_4PbBr_6 (PDF)

■ AUTHOR INFORMATION

Corresponding Authors

Ru-Shi Liu − *Department of Chemistry, National Taiwan University, Taipei 106, Taiwan;* orcid.org/0000-0002-1291-9052; Email: rsliu@ntu.edu.tw

Wuzong Zhou − *EaStChem, School of Chemistry, University of St Andrews, St Andrews KY16 9ST Fife, U.K.;* orcid.org/0000-0001-9752-7076; Email: wzhou@st-andrews.ac.uk

Authors

Weihao Sun − *EaStChem, School of Chemistry, University of St Andrews, St Andrews KY16 9ST Fife, U.K.*

Yuan-Ting Hung − *Department of Chemistry, National Taiwan University, Taipei 106, Taiwan*

Wen-Tse Huang − *Department of Chemistry, National Taiwan University, Taipei 106, Taiwan*

Complete contact information is available at: https://pubs.acs.org/10.1021/acs.cgd.3c01226

Notes

The authors declare no competing financial interest.

■ ACKNOWLEDGMENTS

WS would like to thank the China Scholarships Council and the University of St Andrews for the CSC-St Andrews studentship. Part of this work was financially supported by the National Science and Technology Council in Taiwan (Contract No. NSTC 112-2113-M-002-020) for RSL.

■ REFERENCES

(1) Protesescu, L.; Yakunin, S.; Bodnarchuk, M. I.; Krieg, F.; Caputo, R.; Hendon, C. H.; Yang, R. X.; Walsh, A.; Kovalenko, M. V. Nanocrystals of cesium lead halide perovskites ($CsPbX_3$, X = Cl, Br, and I): novel optoelectronic materials showing bright emission with wide color gamut. *Nano Lett.* **2015**, *15*, 3692−3696.

(2) Chen, J.; Liu, D.; Al-Marri, M. J.; Nuuttila, L.; Lehtivuori, H.; Zheng, K. Photo-stability of $CsPbBr_3$ perovskite quantum dots for optoelectronic application. *Sci. China Mater.* **2016**, *59*, 719−727.

(3) Wang, X.; Bao, Z.; Chang, Y. C.; Liu, R. S. Perovskite quantum dots for application in high color gamut backlighting display of light-emitting diodes. *ACS Energy Lett.* **2020**, *5*, 3374−3396.

(4) Bao, Z.; Wang, W.; Tsai, H. Y.; Wang, H. C.; Chen, S.; Liu, R. S. Photo-/electro-luminescence enhancement of $CsPbX_3$ (X = Cl, Br, or I) perovskite quantum dots via thiocyanate surface modification. *J. Mater. Chem. C* **2020**, *8*, 1065−1071.

(5) Wang, H. C.; Bao, Z.; Tsai, H. Y.; Tang, A. C.; Liu, R. S. Perovskite quantum dots and their application in light-emitting diodes. *Small* **2018**, *14*, No. 1702433.

(6) Otero-Martínez, C.; Fiuza-Maneiro, N.; Polavarapu, L. Enhancing the intrinsic and extrinsic stability of halide perovskite nanocrystals for efficient and durable optoelectronics. *ACS Appl. Mater. Interfaces* **2022**, *14*, 34291−34302.

(7) Hong, Q. M.; Xu, R. P.; Jin, T. Y.; Tang, J. X.; Li, Y. Q. Unraveling the light-induced degradation mechanism of $CH_3NH_3PbI_3$ perovskite films. *Org. Electron.* **2019**, *67*, 19−25.

(8) Fu, Q.; Tang, X.; Huang, B.; Hu, T.; Tan, L.; Chen, L.; Chen, Y. Recent progress on the long-term stability of perovskite solar cells. *Adv. Sci.* **2018**, *5*, No. 1700387.

(9) Akkerman, Q. A.; Abdelhady, A. L.; Manna, L. Zero-dimensional cesium lead halides: history, properties, and challenges. *J. Phys. Chem. Lett.* **2018**, *9*, 2326−2337.

(10) Seth, S.; Samanta, A. Fluorescent phase-pure zero-dimensional perovskite-related Cs_4PbBr_6 microdisks: synthesis and single-particle imaging study. *J. Phys. Chem. Lett.* **2017**, *8*, 4461−4467.

(11) De Bastiani, M.; Dursun, I.; Zhang, Y.; Alshankiti, B. A.; Miao, X.-H.; Yin, J.; Yengel, E.; Alarousu, E.; Turedi, B.; Almutlaq, J. M.; Saidaminov, M. I.; Mitra, S.; Gereige, I.; AlSaggaf, A.; Zhu, Y.; Han, Y.; Roqan, I. S.; Bredas, J.-L.; Mohammed, O. F.; Bakr, O. M. Inside perovskites: quantum luminescence from bulk Cs_4PbBr_6 single crystals. *Chem. Mater.* **2017**, *29*, 7108−7113.

(12) Yu, X.; Wu, L.; Hu, H.; Chen, M.; Tan, Y.; Yang, D.; Pan, Q.; Zhong, Q.; Supasai, T.; Zhang, Q. Cs_4PbX_6 (X = Cl, Br, I) nanocrystals: preparation, water-triggered transformation behavior, and anti-counterfeiting application. *Langmuir* **2018**, *34*, 10363−10370.

(13) Akkerman, Q. A.; Park, S.; Radicchi, E.; Nunzi, F.; Mosconi, E.; De Angelis, F.; Brescia, R.; Rastogi, P.; Prato, M.; Manna, L. Nearly monodisperse insulator Cs_4PbX_6 (X = Cl, Br, I) nanocrystals, their mixed halide compositions, and their transformation into $CsPbX_3$ nanocrystals. *Nano Lett.* **2017**, *17*, 1924−1930.
(14) Mohammed, O. F. Outstanding challenges of zero-dimensional perovskite materials. *J. Phys. Chem. Lett.* **2019**, *10*, 5886−5888.
(15) Thumu, U.; Piotrowski, M.; Owens-Baird, B.; Kolen'ko, Y. V. Zero-dimensional cesium lead halide perovskites: phase transformations, hybrid structures, and applications. *J. Solid State Chem.* **2019**, *271*, 361−377.
(16) Xiang, Q.; Zhou, B.; Cao, K.; Wen, Y.; Li, Y.; Wang, Z.; Jiang, C.; Shan, B.; Chen, R. Bottom up stabilization of $CsPbBr_3$ quantum dots-silica sphere with selective surface passivation via atomic layer deposition. *Chem. Mater.* **2018**, *30*, 8486−8494.
(17) Wang, K.-H.; Wu, L.; Li, L.; Yao, H.-B.; Qian, H.-S.; Yu, S.-H. Large-scale synthesis of highly luminescent perovskite-related $CsPb_2Br_5$ nanoplatelets and their fast anion exchange. *Angew. Chem., Int. Ed.* **2016**, *55*, 8328−8332.
(18) Rossi, C.; Scarfiello, R.; Brescia, R.; Goldoni, L.; Caputo, G.; Carbone, L.; Colombara, D.; De Trizio, L.; Manna, L.; Baranov, D. Exploiting the transformative features of metal halides for the synthesis of $CsPbBr_3@SiO_2$ core−shell nanocrystals. *Chem. Mater.* **2022**, *34*, 405−413.
(19) Xu, J.; Huang, W.; Li, P.; Onken, D. R.; Dun, C.; Guo, Y.; Ucer, K. B.; Lu, C.; Wang, H.; Geyer, S. M.; Williams, R. T.; Carroll, D. L. Imbedded nanocrystals of $CsPbBr_3$ in Cs_4PbBr_6: kinetics, enhanced oscillator strength, and application in light-emitting diodes. *Adv. Mater.* **2017**, *29*, No. 1703703.
(20) Quan, L. N.; Quintero-Bermudez, R.; Voznyy, O.; Walters, G.; Jain, A.; Fan, J. Z.; Zheng, X.; Yang, Z.; Sargent, E. H. Highly emissive green perovskite nanocrystals in a solid state crystalline matrix. *Adv. Mater.* **2017**, *29*, No. 1605945.
(21) Bao, Z.; Tseng, Y.-J.; You, W.; Zheng, W.; Chen, X.; Mahlik, S.; Lazarowska, A.; Lesniewski, T.; Grinberg, M.; Ma, C.; Sun, W.; Zhou, W. Z.; Liu, R.-S.; Attfield, J. P. Efficient luminescence from $CsPbBr_3$ nanoparticles embedded in Cs_4PbBr_6. *J. Phys. Chem. Lett.* **2020**, *11*, 7637−7642.
(22) Bao, Z.; Hsiu, C.-Y.; Fang, M.-H.; Majewska, N.; Sun, W. H.; Huang, S.-J.; Yuan, E. C.-Y.; Chang, Y.-C.; Chan, J. C. C.; Mahlik, S.; Zhou, W. Z.; Yang, C.-W.; Lu, K.-M.; Liu, R.-S. Formation and near-infrared emission of $CsPbI_3$ nanoparticles embedded in Cs_4PbI_6 crystals. *ACS Appl. Mater. Interface* **2021**, *13*, 34742−34751.
(23) Li, Y.; Huang, H.; Xiong, Y.; Kershaw, S. V.; Rogach, A. L. Reversible transformation between $CsPbBr_3$ and Cs_4PbBr_6 nanocrystals. *CrystEngComm* **2018**, *20*, 4900−4904.
(24) Hu, G.; Qin, W.; Liu, M.; Ren, X.; Wu, X.; Yang, L.; Yin, S. Scalable room-temperature synthesis of plum-pudding-like Cs_4PbBr_6/$CsPbBr_3$ microcrystals exhibiting excellent photoluminescence. *J. Mater. Chem. C* **2019**, *7*, 4733−4739.
(25) Xuan, T.; Lou, S.; Huang, J.; Cao, L.; Yang, X.; Li, H.; Wang, J. Monodisperse and brightly luminescent $CsPbBr_3/Cs_4PbBr_6$ perovskite composite nanocrystals. *Nanoscale* **2018**, *10*, 9840−9844.
(26) Li, X.; Wu, Y.; Zhang, S.; Cai, B.; Gu, Y.; Song, J.; Zeng, H. $CsPbX_3$ quantum dots for lighting and displays: room-temperature synthesis, photoluminescence superiorities, underlying origins and white light-emitting diodes. *Adv. Funct. Mater.* **2016**, *26*, 2435−2445.
(27) Aebli, M.; Benin, B. M.; McCall, K. M.; Morad, V.; Thöny, D.; Grützmacher, H.; Kovalenko, M. V. White $CsPbBr_3$: characterizing the one-dimensional cesium lead bromide polymorph. *Helv. Chim. Acta* **2020**, *103*, No. e2000080.
(28) Greer, H. F.; Zhou, W. Z. Electron diffraction and HRTEM imaging of beam sensitive materials. *Crystallogr. Rev.* **2011**, *17*, 163−185.
(29) Xiao, B.; Byrne, P. J.; Wheatley, P. S.; Wragg, D. S.; Zhao, X. B.; Fletcher, A. J.; Thomas, M.; Peters, L.; Evans, J. S. O.; Warren, J. E.; Zhou, W. Z.; Morris, R. E. Chemically blockable transformation and ultra-selective low pressure gas adsorption in a non-porous metal organic framework. *Nat. Chem.* **2009**, *1*, 289−294.
(30) Wright, P. A.; Zhou, W. Z.; Perez-Pariente, J.; Arranz, M. Direct observation of growth defects in zeolite beta. *J. Am. Chem. Soc.* **2005**, *127*, 494−495.
(31) Geng, J. F.; Zhou, W. Z.; Skelton, P.; Yue, W. B.; Kinloch, I. A.; Windle, A. H.; Johnson, B. F. G. Crystal structure and growth mechanism of unusually long fullerene (C_{60}) nanowires. *J. Am. Chem. Soc.* **2008**, *130*, 2527−2534.
(32) Snyder, L. R.; Kirkland, J. J.; Glajch, J. L. *Practical HPLC Method Development*, 2nd ed.; John Wiley & Sons Inc, 1997.
(33) Cavanaugh, J.; Whittaker, M. L.; Joester, D. Crystallization kinetics of amorphous calcium carbonate in confinement. *Chem. Sci.* **2019**, *10*, 5039−5043.
(34) Demichelis, R.; Raiteri, P.; Gale, J. D.; Quigley, D.; Gebauer, D. Stable prenucleation mineral clusters are liquid-like ionic polymers. *Nat. Commun.* **2011**, *2*, No. 590.
(35) Zhang, Y.; Saidaminov, M. I.; Dursun, I.; Yang, H.; Murali, B.; Alarousu, E.; Yengel, E.; Alshankiti, B. A.; Bakr, O. M.; Mohammed, O. F. Zero-dimensional Cs_4PbBr_6 perovskite nanocrystals. *J. Phys. Chem. Lett.* **2017**, *8*, 961−965.

https://doi.org/10.1021/acs.cgd.3c01226
Cryst. Growth Des. 2024, 24, 545−553